Article | Open Access

Energy Materials

Lei *et al. Energy Mater.* **2026**, *6*, 600136 **DOI:**10.20517/energymater.2026.213

Pyridine derivatives desorb physisorbed multilayers from dip-coated self-assembled monolayers for scalable and efficient perovskite solar cells

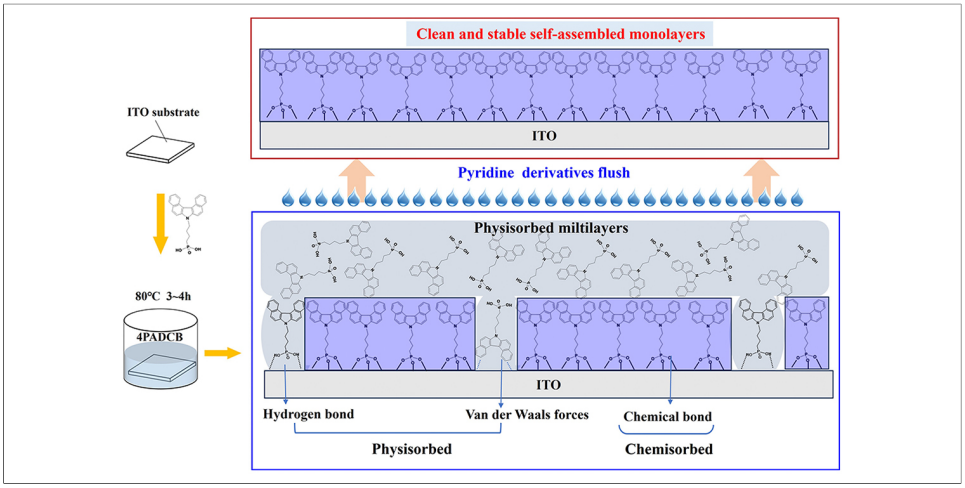
Yajie Lei[1,#], Qing Zhong[1,#], Jinbo Chen[1,2,*], Luyao Hao[1], Kaixin Huang[1], Yizhou Qian[1], Xiangcheng Li[1], Jiajia Yuan[1], Jiaxin Zhang[1], Hanjian Lai[1], Xianyong Zhou[1,2], Bin-Bin Yu[1], Wai-Yeung Wong[3,*], Xingzhu Wang[1,*], Chang Liu[1,2,*]

Keywords:
Perovskite solar cells, self-assembled monolayers, dip-coating, pyridine derivatives, scalable fabrication

Citation: Lei, Y.; Zhong, Q.; Chen, J.; Hao, L.; Huang, K.; Qian, Y.; Li, X.; Yuan, J.; Zhang, J.; Lai, H.; Zhou, X.; Yu, B. B.; Wong, W. Y.; Wang, X.; Liu, C. Pyridine derivatives desorb physisorbed multilayers from dip-coated self-assembled monolayers for scalable and efficient perovskite solar cells. *Energy Mater.* **2026**, *6*, 600136. https://dx.doi.org/10.20517/energymater.2026.213

Received: 8 Jul 2026
First Decision: 10 Aug 2026
Revised: 24 Aug 2026
Accepted: 10 Sep 2026
Published: 21 Oct 2026

Academic Editor:
Meicheng Li
Copy Editor:
Shu-Yuan Duan
Production Editor:
Shu-Yuan Duan



Abstract

Phosphonic acid-based self-assembled monolayers (SAMs) are widely used as hole-selective contacts in inverted perovskite solar cells. However, conventional deposition methods of SAMs inevitably leave physisorbed multilayers that contain under-protonated P-OH groups, which degrade the buried interface and hinder carrier extraction. Here, we report a dip-flush strategy using pyridine derivatives (3-fluoropyridine and 3-methoxypyridine) as mild coordinating solvents to selectively remove weakly bound species from dip-coated 4-(7H-dibenzo[c,g]carbazol-7-yl)butyl phosphonic acid SAMs. These pyridine derivatives exploit strong hydrogen-bond-accepting ability to preferentially interact with physisorbed molecules, thereby desorbing aggregates while leaving the chemisorbed monolayer intact. Density functional theory calculations confirm that 3-methoxypyridine exhibits superior cleaning efficacy owing to its stronger binding affinity and lower removal energy. The flush post-treatment significantly reduces residual P-OH groups and yields a cleaner, more hydrophobic, and smoother SAM surface. Consequently,

[1]Engineering and Research Center for Integrated New Energy Photovoltaics & Energy Storage Systems of Hunan Province, School of Electrical Engineering, University of South China, Hengyang 421001, Hunan, China.
[2]Hunan Chang-rui New Energy Limited Company, Hengyang 421001, Hunan, China.
[3]The Hong Kong Polytechnic University Shenzhen Research Institute, Shenzhen 518000, Guangdong, China.
[#]These authors contributed equally to this work.

[*]**Correspondence to:** Prof. Chang Liu, Xingzhu Wang, Jinbo Chen, Engineering and Research Center for Integrated New Energy Photovoltaics & Energy Storage Systems of Hunan Province, School of Electrical Engineering, University of South China, Hengyang 421001, Hunan, China. E-mail: liuchang@usc.edu.cn; wangxz@sustech.edu.cn; chenjb16@usc.edu.cn. Prof. Wai-Yeung Wong, The Hong Kong

Polytechnic University Shenzhen Research Institute, Shenzhen 518000, Guangdong, China. E-mail: wai-yeung.wong@polyu.edu.hk

perovskite films grown on the cleaned SAM show enhanced crystallinity and a void-free buried interface. As a result, the optimized dip-flush SAM delivers a champion power conversion efficiency of 26.49%, and this advantage scales up to a 12.87 cm^2 (aperture area) mini-module, for which a PCE of 22.56% is obtained. This dip-flush chemically selective strategy offers a scalable pathway toward highperformance, largearea perovskite photovoltaics.

INTRODUCTION

Self-assembled monolayers (SAMs) have become indispensable interfacial materials in optoelectronics, particularly in the rapidly advancing field of perovskite solar cells (PSCs)[1-3]. In inverted (p-i-n) PSCs, SAMs serve as an ultra-thin selective contact layer that not only improves holes extract efficiency but also passivates defects at the buried interface between the transparent conductive oxide (TCO) and the perovskite absorber[4-6]. A wide variety of SAMs have been explored, including carboxylic acids (-COOH)-, phosphonic acids (-PO_3H_2)- and boronic acids [-$B(OH)_2$]-based SAMs[7,8]. Among these, phosphonic acids-based SAMs have emerged as the most successful and widely adopted class for perovskite photovoltaics. Their advantages stem from the strong bidentate or tridentate binding to hydroxylated TCO surfaces, such as indium tin oxide (ITO) and fluorine-doped tin oxide (FTO), which provides exceptional thermal and hydrolytic stability.

A typical SAM molecule consists of three functional parts: an anchoring group that chemisorbs to the oxide substrate, a spacer (often an alkyl or conjugated chain), and a terminal group that interfaces with the active layer. Their modular molecular design allows fine-tuning of the terminal group to achieve optimal energy level alignment with the perovskite[9,10]. The self-assembly process occurs spontaneously upon exposure of a clean TCO substrate to a dilute solution of the SAM-forming molecule, driven by the strong affinity between the anchoring group and the hydroxyl groups on the TCO surface. Generally, the amphiphilic nature of SAM molecules leads to significant molecular agglomeration in most organic solvents, forming micelles or disordered clusters[11-13]. Meanwhile, the anchoring groups initially interact with oxide substrates only through weak, reversible adsorption, requiring sufficient time to evolve into stable, densely packed configurations[7,14,15].

Spin-coating is the most commonly used method for SAM deposition on small-area substrates due to its simplicity and good reproducibility[16,17]. However, the rapid solvent evaporation leads to insufficient dissociation of agglomerated SAM molecules, accompanied by the failure of multilayer adsorbed molecules to reorganize into a well-ordered, densely packed monolayer[18-20]. Furthermore, when scaling up to large-area or flexible plastic substrates, the centrifugal force-induced radial non-uniformity and severe edge effects exacerbate these issues, making it extremely difficult to achieve homogeneous and high-quality SAM coatings across the entire device area. To overcome these limitations, static immersion (dip-coating) has been proposed as a promising alternative. In this technique, the substrate is fully immersed in a SAM molecule solution and kept stationary for an extended period. This allows the molecules to dissociate from agglomerates, displace adsorbed species, and gradually reorganize into a densely packed, well-ordered monolayer under near-equilibrium conditions[21-24]. Consequently, static immersion achieves superior surface coverage, molecular ordering, and uniformity - advantages that are particularly critical for large-area and flexible substrates where spin-coating consistently fails to deliver homogeneous SAM coatings.

However, both spin-coating and dip-coating inevitably introduce physisorbed multilayers that carry under-protonated P-OH groups not involved in substrate anchoring. These residual P-OH species at the buried interface catalyze distinct degradation pathways of the perovskite[2,25,26]. Meanwhile, due to the poor hole mobility of SAM molecules, the multilayers themselves hinder carrier extraction. Therefore, a judicious

post-treatment step is essential to remove physisorbed aggregates and weakly bound species without detaching or disrupting the chemisorbed monolayer.

In this work, we propose a rational dip-flush strategy to address the intrinsic limitations of physisorbed multilayers in conventional SAM deposition methods. Specifically, we introduce pyridine derivatives, including 3-fluoropyridine (3-FPy) and 3-methoxypyridine (3-MeOPy), as mild coordinating solvents to selectively remove weakly bound species from dip-coated 4-(7H-dibenzo[c,g]carbazol-7-yl)butyl phosphonic acid (4PADCB) SAMs on ITO substrates. These pyridine derivatives possess strong hydrogen-bond-accepting ability, which allows them to preferentially interact with the phosphonic acid groups of physisorbed 4PADCB molecules. Density functional theory (DFT) calculations reveal that 3-MeOPy exhibits the lowest binding energy to 4PADCB and the lowest removal energy, confirming its superior efficacy in eliminating residual multilayers. Consequently, they desorb aggregates anchored by weak van der Waals forces and hydrogen bonds, while leaving the chemically anchored monolayer intact. This selective removal process yields a clean, well-ordered, and fully anchored SAM surface with markedly reduced P-OH residues. Consequently, the optimized dip-flush SAM enables a champion power conversion efficiency of 26.49% for small-area devices. It also exhibits a power conversion efficiency (PCE) of 22.56% for a 12.87 cm^2 mini-module, demonstrating that this facile yet chemically intelligent strategy offers a scalable pathway toward high-performance, large-area perovskite photovoltaics.

EXPERIMENTAL

Materials

We obtained formamidinium iodide (FAI), cesium iodide (CsI), methylammonium chloride (MACl), lead iodide (PbI_2), 4PADCB, 1,3-propanediammonium iodide (PDADI), piperazinium iodide (PI), lead chloride ($PbCl_2$), benzylamine hydroiodide (PMAI) and 3-Methylthio-1-propylammonium iodide (3MTPAI) from Youxuan Co., Ltd., with purities ≥ 99.9% unless otherwise stated. 3-FPy and 3-MeOPy (both 98%) were supplied by Bide Co., Ltd. C_{60} and bathocuproine (BCP) were purchased from Xi'an Polymer Light Technology Co., Ltd. Anhydrous solvents including N,N-Dimethylformamide (DMF), Dimethyl sulfoxide (DMSO), N-methyl-2-pyrrolidone (NMP), chlorobenzene, and isopropanol (IPA) were acquired from Sigma-Aldrich, while copper was purchased from China National Medicines Chemical Reagents Co., Ltd.

Perovskite solar cell device fabrication:

Small-area devices fabrication: A 1.6 M $FA_{0.95}Cs_{0.05}PbI_3$ precursor solution was prepared by dissolving FAI, CsI, PbI_2, and MACl in a co-solvent mixture of DMSO and DMF (1 mL, volume ratio 1:4) with a molar ratio of 0.95:0.05:1.15:0.2. In addition, PMAI (1.0 mg/mL) was added to the perovskite precursor solution as an additive to further improve film quality. The perovskite precursor was prepared by stirring overnight and then filtered through a 0.22 μm polytetrafluoroethylene membrane immediately before use. As for the ITO substrates, they underwent successive ultrasonic cleaning in detergent, deionized water, and isopropanol (30 min per step), followed by N_2 blowing and a 30-min UV-ozone treatment. Subsequently, the substrate was immersed in a pre-prepared solution of 4PADCB dissolved in isopropanol (0.5 mg/mL) and soaked at 80 °C for 3-4 h to facilitate the chemical adsorption and bonding of the self-assembled monolayer.

The substrate was then dried with a nitrogen stream and was moved into a nitrogen-filled glovebox, where we rinsed the SAM and proceeded to deposit the perovskite layer or perform post-treatment. 3-FPy or 3-MeOPy was directly applied to the 4PADCB-modified ITO/glass substrate in its undiluted form, without dilution or the addition of any carrier solvent. The neat pyridine derivative was spin-coated at 5,000 rpm for 30 s, followed by annealing at 100 °C for 5 min. The post-annealing step following the spin-coating of pyridine derivatives was applied solely to accelerate the removal of residual pyridine species and does not significantly affect the pre-existing SAM layer. Then perovskite films were deposited onto the SAM layer at 5,

000 rpm for 45 s. During the second spin-coating step, chlorobenzene (150 μL) was swiftly dropped onto the spinning substrate as an anti-solvent at an interval of 1 s, 10 s prior to the end of the program. This was followed by thermal annealing at 120 °C for 20 min. After annealing, a mixed solution of PDADI (2 mg·mL^{-1}) and 3MTPAI (2.5 mg·mL^{-1}), pre-dissolved in isopropanol, was dynamically spin-coated onto the perovskite film at 5,000 rpm for 30 s and then thermally annealed at 100 °C for 5 min. Subsequently, the prepared substrates were transferred to deposit a 30 nm C_{60} layer (deposition rate: 0.03 nm/s), an 8 nm BCP layer (deposition rate: 0.02 nm/s), and a 100 nm Cu electrode, which were sequentially deposited via thermal evaporation to complete the perovskite solar cell devices.

Modules fabrication: For the 5 ×5 cm^2 module, the substrate was immersed in a 4PADCB solution in isopropanol (0.5 mg/mL) and kept at 80 °C for 3-4 h. Afterward, the substrate was transferred into a nitrogen-filled glovebox, where its surface was rinsed with 200 μL of 3-MeOPy at 5,000 rpm for 30 s. The substrate was then annealed at 100 °C for 5 min. 300 μL perovskite solution (570.94 mg FAI, 176.68 mg CsI, 1,844.04 mg PbI_2, and 111.24 mg $PbCl_2$ were dissolved in a mixture solution of 2 mL DMF and 384 μL NMP) was spin-coated onto the SAM layer at 4,000 rpm for 50 s (1,000 rpm·s^{-1} of acceleration), followed by annealing at 150 °C for 10 min. 180 μL PI (0.4mg/mL) solution was spin-coated on the perovskite film at 4,000 rpm for 30 s (2,000 rpm·s^{-1} of acceleration), followed by annealing at 100 °C for 10 min. The device fabrication was accomplished by sequentially thermal evaporating C_{60} (25 nm, deposition rate: 0.03 nm/s), BCP (5 nm, 0.02 nm/s), and Cu (100 nm, 0.1 nm/s) in a vacuum chamber. Laser-patterned lines (P1, P2, and P3) were accomplished by the 355nm laser beam with a scribing speed of 200 mm·s^{-1}. The scribing powers of P1, P2, and P3 are 0.4, 0.3, and 0.3 W, respectively. The scribing frequencies of P1, P2, and P3 are 500, 62.5, and 83.3 kHz, respectively. The line widths of P1, P2 and P3 are about 25, 50 and 37.5 μm, respectively. The line spacing between P1 and P2, and P2 and P3 is about 60 μm. The aperture area of the module is about 12.87 cm^2.

Characterization methods

The current density-voltage (*J-V*) curves were recorded with a Keithley 2400 Source Measure Unit, while the devices were exposed to simulated AM1.5G solar radiation (100 mW cm^{-1}) from an LST-S-55 simulator (LightSky Technology, xenon lamp). Measurements were performed inside a nitrogen glove box, using non-encapsulated cells and a shadow mask that confined the illuminated area to 0.0736 cm^2. Both reverse-scan (1.2 to -0.1 V, step 0.02 V) and forward-scan (-0.1 to 1.2 V, step 0.02 V) measurements were carried out with a 1-ms delay time. The *J–V* curves of the mini-modules were measured under AM 1.5G illumination (100 mW cm^{-2}). Both reverse-scan (9.6 V to –0.1 V, step 0.05 V) and forward-scan (–0.1 V to 9.6 V, step 0.05 V) measurements were carried out with a 1-ms delay time. Calibration of the solar irradiance was performed using a certified silicon diode (LRC-KG5-013, LightSky Technology), while EQE data were collected via the LST-QE system supplied by the same manufacturer. We acquired steady-state and time-resolved photoluminescence (PL and TRPL) using an FLS1000 spectrometer (Edinburgh Instruments) at 470 nm excitation, and obtained scanning electron microscopy (SEM) micrographs with a SU8010 field-emission instrument. X-ray diffraction (XRD) patterns were collected on a Rigaku Smart Lab SE diffractometer (Cu Kα, 40 kV/40 mA) at a scanning rate of 10° min^{-1}. For surface chemical and electronic analysis, we employed a Thermo Scientific ESCALab250 system, where X-ray photoelectron spectroscopy (XPS) spectra were charge-corrected to the C 1s signal at 284.80 eV, and ultraviolet photoelectron spectroscopy (UPS) data were also recorded. Atomic force microscopy (AFM) measurements were finally performed on a Bruker device.

Computation details

All DFT calculations, carried out with VASP and the PBE functional plus Grimme's D3 correction, used a 550 eV plane-wave cutoff for valence electrons and PAW potentials for cores[27-31]. Owing to the large supercell, Γ-point sampling was applied throughout.

The ITO surface, modeled by the (111) facet of In_2O_3 given the low Sn doping concentration, was adopted from the work of Fei et al. and subsequently re-optimized within VASP[25]. To avoid artificial interactions between periodically repeated slabs, a 30 Å vacuum layer was introduced perpendicular to the surface (along *z*). An on-site Hubbard correction (DFT + U, U = 3.0 eV) was applied to the In 4d semicore states to properly localize these electrons and improve the description of the electronic structure, following previously established parameters for In_2O_3[32]. For adsorption studies, all SAM adsorbates and the top two atomic layers of the ITO slab were fully relaxed during geometry optimization, with convergence thresholds set to residual forces below 0.05 eV $Å^{-1}$. The binding energy (ΔE_b) of 3-FPy-4PADCB and 3-MeOPy-4PADCB dimers was calculated using:

$$\Delta E_b = E_{SAM-M} - E_{SAM} - E_M \quad (1)$$

where E_{SAM-M}, E_{SAM}, and E_M represent the total energies of the 4PADCB-solvents (pyridine derivatives) dimer, the isolated 4PADCB molecule, and the free solvent molecule, respectively[33]. To evaluate the removal energetics, two distinct adsorption configurations of the SAM molecule on the In_2O_3 (111) surface were considered. In the first, the molecule was placed perpendicular to the surface to enable hydrogen bonding between the phosphonic acid group and the surface hydroxyls; in the second, it was oriented parallel to the surface to facilitate direct interactions between the carbazole moiety and the oxide substrate. Both configurations were fully relaxed using DFT to obtain their respective ground-state energies. The corresponding removal energies for displacing the adsorbed 4PADCB species with 3-FPy and 3-MeOPy were then computed according to:

$$\Delta E_{removal} = (E_{SAM-M} + E_{In_2O_3}) - (E_M + E_{SAM^*}) \quad (2)$$

where E_{SAM-M} and E_M are the total energies of the SAM-pyridine derivatives dimer and the free solvent molecule, and $E_{In_2O_3}$ and E_{SAM^*} denote the energies of the pristine In_2O_3 slab and the SAM-adsorbed In_2O_3 surface, respectively[25,33]. The different schematics of the adsorption modes can be found in Supplementary Figures 1 and 2.

RESULTS AND DISCUSSION

As illustrated in Figure 1A, the dip-flush method involves two sequential steps. First, the TCO substrate is immersed in a 4PADCB solution (with isopropanol as the solvent) for a predetermined period to facilitate SAM deposition via dip-coating. Subsequently, the substrate is rinsed with a pyridine-based solvent, which selectively removes weakly bound physisorbed species while preserving the integrity of the chemisorbed monolayer. For comparison, control samples were prepared using only the dip-coating step without the subsequent flush. The surface wettability of ITO substrates modified under these two conditions was evaluated by sessile drop contact angle measurements. The control SAM surface (dip-coating only) exhibited a contact angle of 68.9° [Figure 1B]. In contrast, after the pyridine derivatives flush, the contact angle increased to approximately 80.9° for 3-FPy and 86.7° for 3-MeOPy (Figure 1C and D, respectively). It is well established that the terminal group of 4PADCB is hydrophobic, whereas the phosphonic acid anchoring group is hydrophilic. The marked increase in hydrophobicity following the flush indicates that the pyridine treatment effectively removes residual physisorbed multilayers and irregularly oriented SAM molecules, thereby exposing a cleaner, better-ordered monolayer with the hydrophobic terminal groups facing outward.

XPS analysis was conducted to probe the surface chemistry of ITO substrates modified with dip-coated SAMs before and after post-treatment. Supplementary Figure 3 presents the survey spectra in the F 1s region for samples subjected to 3-FPy treatment, both before and after the post-treatment step. The absence of any detectable F 1s peaks in either spectrum confirms that the pyridine derivatives post-treatment does not

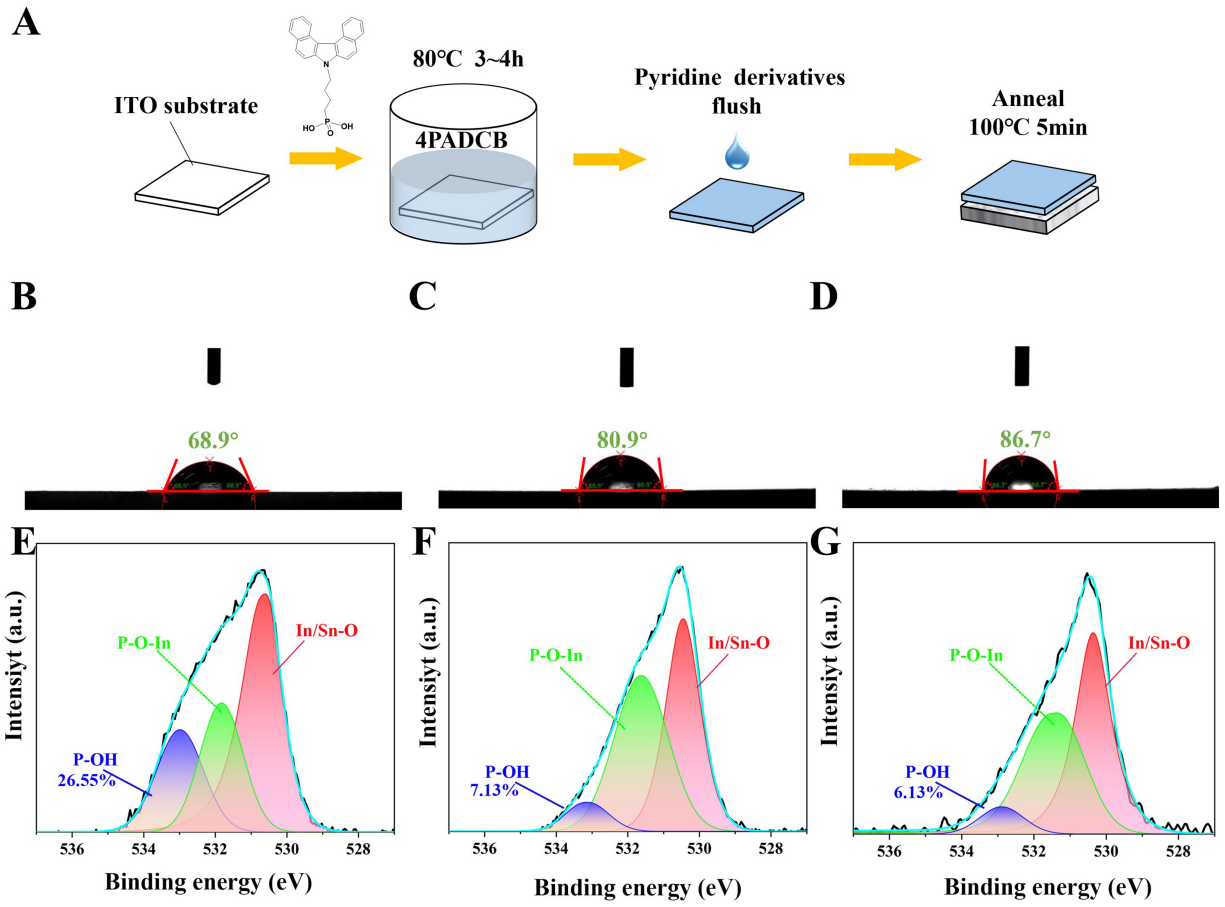


Figure 1. (A) Schematic illustration of the deposition process via the dip-flush method; (B-D) Water contact angles on SAM-modified ITO substrates: (B) control (dip-coated only), (C) 3-FPy post-treatment, and (D) 3-MeOPy post-treatment; (E-G) O 1s XPS core-level spectra of the corresponding SAM surfaces: (E) control, (F) 3-FPy post-treatment, and (G) 3-MeOPy post-treatment. ITO: Indium tin oxide; 4PADCB: 4-(7H-dibenzo[c,g]carbazol-7-yl)butyl phosphonic acid; SAM: self-assembled monolayer; XPS: X-ray photoelectron spectroscopy; 3-FPy: 3-fluoropyridine; 3-MeOPy: 3-methoxypyridine.

introduce residual solvent contamination on the substrate surface. We further analyzed the ratio of adsorbed P-OH groups on the ITO surface by evaluating the peak areas in the O 1s core level XPS spectra [Figure 1E-G]. The O 1s spectrum was deconvoluted into three peaks at 532.99, 531.82, and 530.59 eV, corresponding to P-OH, P-O-In, and In/Sn-O, respectively[6,34]. The P-OH ratio was 26.55% for the control sample, decreasing to 7.13% after 3-FPy treatment and to 6.13% after 3-MeOPy treatment. To further confirm that the observed changes arise from the displacement of weakly adsorbed species by pyridine derivatives rather than from thermal effects during the post-annealing step, we performed control experiments with and without annealing. As shown in Supplementary Figure 4, neither the annealing of pyridine-treated SAM substrates nor the annealing of dip-coated SAM substrates without flush significantly altered the O 1s spectral features or the relative P-OH intensity. In addition, we performed control experiments using IPA and DMSO as alternative post-treatment solvents under identical conditions [Supplementary Figure 5]. The results revealed that the P-OH ratio decreased to 12.60% for IPA and 16.11% for DMSO, confirming the superior ability of the pyridine derivative to displace physisorbed multilayers. These results confirm that the pyridine flush removes a substantial portion of residual physisorbed multilayers and irregularly oriented SAM molecules from the surface. Importantly, the persistence of the P-O-In peak demonstrates that the post-treatment does not damage the chemisorbed monolayer.

As illustrated in Figure 2A, dip-coated 4PADCB alone tends to form disordered multilayers on ITO due to steric hindrance and molecular aggregation. This leads to poor molecular packing, hindered carrier transport

, and compromised buried interface stability. In contrast, post-treatment with pyridine derivatives removes these physisorbed multilayers, leaving behind a well-ordered, chemisorbed monolayer with near-complete substrate coverage. To directly evaluate the quality and homogeneity of the SAM layer formed via the dip-flush approach, we employed AFM to characterize the surface topography of both the reference and post-treated substrates. As depicted in Figure 2B-D, the sample prepared solely by dip coating yielded a root-mean-square (RMS) roughness of 3.64 nm. In contrast, post-treatment with 3-FPy reduced the surface roughness to 2.96 nm, while the use of 3-MeOPy led to an even lower value of 2.81 nm, indicating a more effective removal of physisorbed multilayers by the methoxy-substituted pyridine derivative. Besides, as shown in the AFM section analyses [Supplementary Figures 6-8], the control SAM surface exhibits numerous nanoscale protrusions with lateral dimensions of 10-20 nm, which are attributed to molecular aggregation and the presence of physisorbed multilayers. In contrast, following the pyridinebased flush treatment, these aggregates are entirely eliminated, leaving behind a smooth and wellordered SAM surface that is free of residual clusters. This progressive reduction in surface roughness and nanoscale protrusions confirms the effective removal of physisorbed multilayers, which is consistent with the well-established correlation that higher molecular packing density leads to smoother surface topographies[35,36].

To further understand the selective removal ability of different pyridine derivatives, DFT calculations were performed. Both 3-FPy and 3-MeOPy are polar aprotic solvents with strong hydrogen-bond-accepting ability but no hydrogen-bond-donating capacity. Compared with 3-FPy, the electron-donating methoxy group in 3-MeOPy increases the electron density on the pyridine ring, as reflected in their electrostatic surface potential (ESP) maps (top, Figure 2E and F). It is well established that chemisorbed 4PADCB molecules are tightly bound to the ITO surface via phosphonic acid anchoring and are difficult to remove[33,37]. In contrast, physisorbed species, which are attached through weaker interactions such as hydrogen bonding or van der Waals forces, can be more readily displaced. To quantify the interaction strength between the pyridine derivatives and 4PADCB, we construct pyridine 4PADCB dimers configurations (bottom, Figure 2E and F) and calculated the binding energies of the corresponding dimers. The computed binding energies are -0.46 eV for 3-FPy-4PADCB and -0.57 eV for 3-MeOPy-4PADCB, indicating that 3-MeOPy exhibits a stronger affinity toward 4PADCB, which rationalizes its superior efficacy in removing physisorbed multilayers.

On ITO surfaces, physisorbed 4PADCB molecules adopt two distinct binding modes: hydrogen bonding via the phosphonic acid -OH group, and weaker interactions through the terminal carbazole moiety. The perpendicular geometry maximizes the directional O-H···O hydrogen bond, while the parallel geometry maximizes the contact area between the molecular backbone and the surface, thereby capturing the dominant dispersive component. To differentiate these modes by their susceptibility to solvent rinsing, we performed DFT calculations to evaluate the removal energy, defined as the energy required to desorb a molecule from the surface [Figure 2G]. For hydrogen-bonded species, the removal energy decreases from 0.82 eV with 3-FPy to 0.71 eV with 3-MeOPy, with the lower value indicating easier detachment. This reduction reflects the stronger hydrogen-bond-accepting ability of 3-MeOPy, conferred by its electron-donating methoxy group. In contrast, carbazole-bound molecules exhibit systematically higher removal energies (0.99 eV for 3-FPy and 0.88 eV for 3-MeOPy), indicating that they are more tenaciously attached, regardless of the solvent. Nevertheless, 3-MeOPy still outperforms 3-FPy in dislodging both types of physisorbed species, underscoring its superior capacity to clean the SAM-covered ITO surface.

To better understand the connection between SAM-treated ITO surface texture and the crystal growth of perovskite films, we carried out SEM analyses on perovskite film samples prepared with different substrates. Figure 3A-C displays the top-view SEM micrographs of perovskite films grown on ITO/SAM. Evidently, the perovskite layers prepared on dip-flushed substrates exhibit notably larger grain sizes than those on the untreated control, with the corresponding grain-size distributions summarized in Supplementary Figure 9.

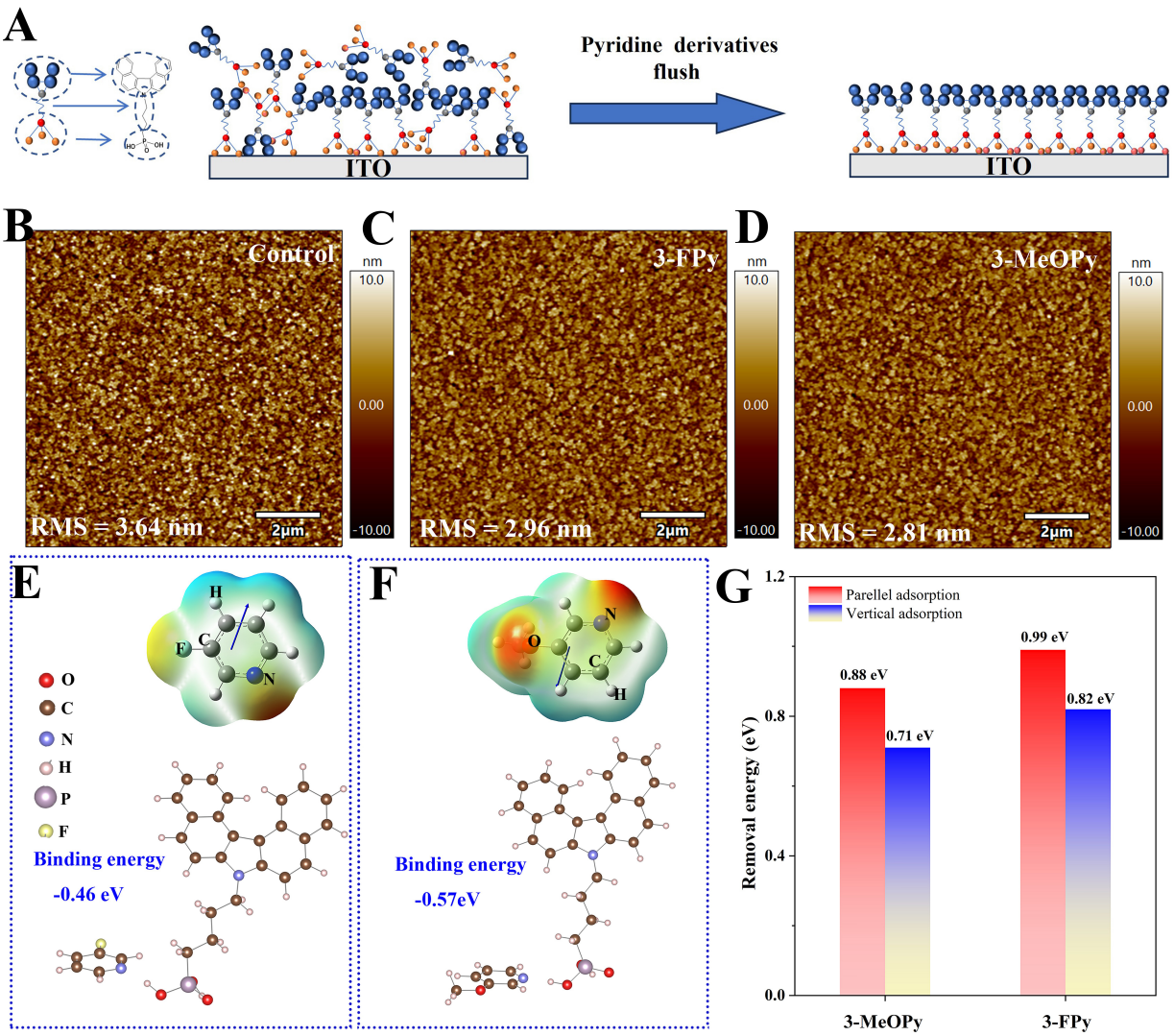


Figure 2. (A) Schematic illustration of the pyridine-based flush process for removing physisorbed multilayers from the SAM-coated ITO surface. From top to bottom, the first arrow corresponds to the "7H-dibenzo[c,g]carbazole unit", the second arrow corresponds to the "Alkyl spacer chain", and the third arrow corresponds to the "Phosphonic acid anchoring group"; (B-D) AFM topography images of SAM surfaces: (B) control (dip-coated only), (C) after 3-FPy post-treatment, and (D) after 3-MeOPy post-treatment; (E and F) ESP maps (top) and corresponding molecular structures (bottom) of (E) 3-FPy-4PADCB and (F) 3-MeOPy-4PADCB dimers; (G) DFT-calculated removal energies for displacing adsorbed 4PADCB using 3-FPy and 3-MeOPy. ITO: Indium tin oxide; SAM: self-assembled monolayer; 4PADCB: 4-(7H-dibenzo[c,g]carbazol-7-yl)butyl phosphonic acid; ESP: electrostatic surface potential; DFT: density functional theory; 3-FPy: 3-fluoropyridine; 3-MeOPy: 3-methoxypyridine.

As for buried interface images [Figure 3D-F], in addition to larger crystalline domains, the dip-flushed sample exhibits a marked reduction in interfacial voids defects that commonly arise from poor SAM coverage and residual physisorbed layers. Figure 3G compares cross-sectional SEM images of perovskite films on control versus dip-flushed SAM substrates, revealing that the latter exhibit continuous large-sized columnar grains and a void-less buried interface - features that demonstrate superior deposition quality and more favorable grain growth. The enhanced performance is ascribed to the removal of the nanoscale aggregates observed in AFM, which otherwise would serve as heterogeneous nucleation sites that disrupt uniform perovskite crystallization. Figure 3H displays the XRD patterns acquired from the perovskite films. In every sample, a small peak appears at 12.7°, which arises from excess PbI_2. After applying the dip-flush treatment, the perovskite-specific reflections at 14.1° and 28.6° exhibit a pronounced intensity rise, pointing to improved crystallinity. This enhancement correlates well with the coarser grain morphology observed in the SEM images.

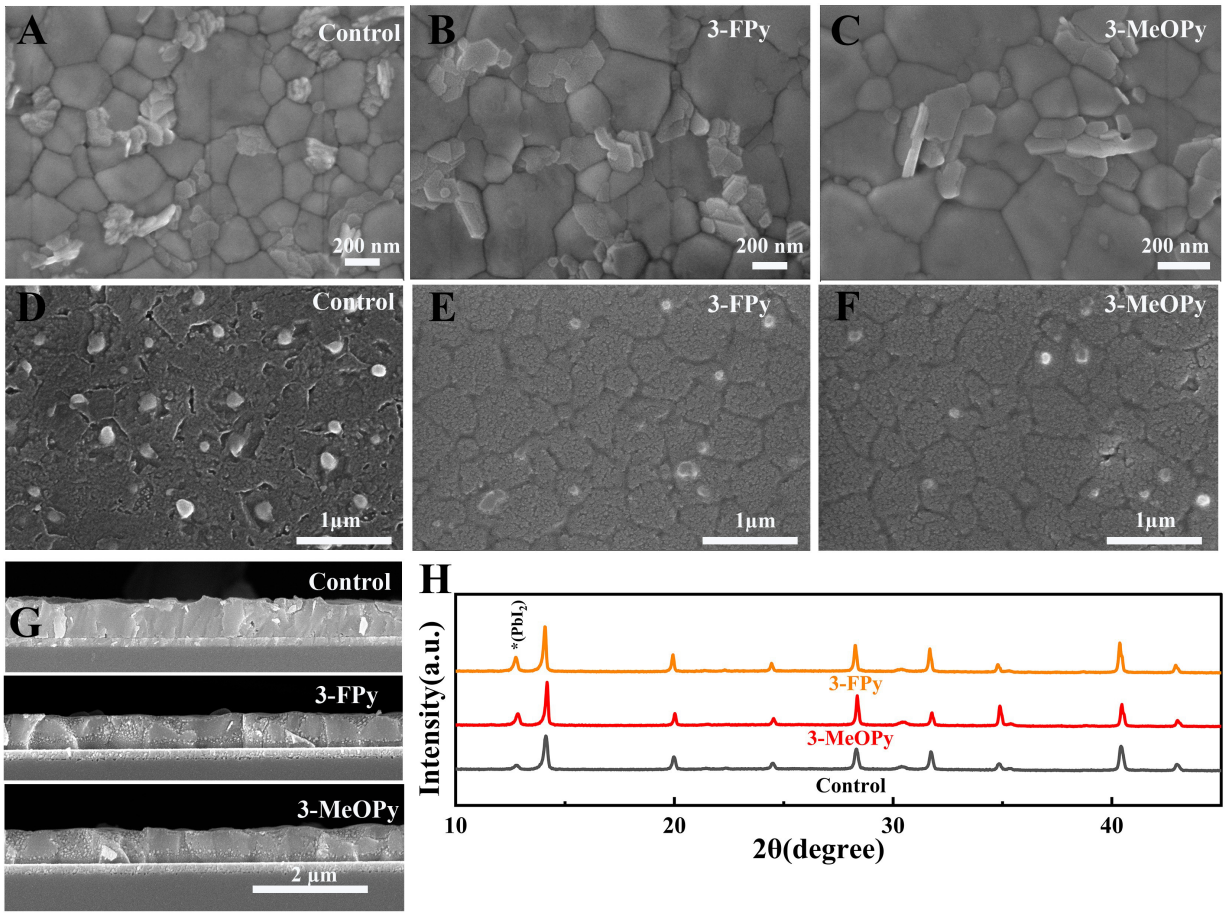


Figure 3. (A-C) Top-view SEM images of perovskite films deposited on (A) the control SAM, (B) the 3-FPy-treated SAM, and (C) the 3-MeOPy-treated SAM; (D-F) Corresponding bottom-view SEM images of the buried perovskite/SAM interfaces; (G) Cross-sectional SEM images of the complete perovskite films on the three substrates; (H) The XRD patterns for perovskite films prepared on different substrates. 3-FPy: 3-fluoropyridine; 3-MeOPy: 3-methoxypyridine; SEM: scanning electron microscopy; SAM: self-assembled monolayer; XRD: X-ray diffraction.

To further characterize how SAM morphology influences the physical and chemical state of the ITO surface and to determine energy band matching with perovskite, we performed XPS focused on the In $3d_{5}/_{2}$ core level and UPS. Shifts in In band energy peak reflect changes in the electronic environment of indium atoms within the ITO substrate, allowing assessment of both the extent of SAM removal and the structural evolution of the SAM after solvent rinsing[37]. As shown in Figure 4A, deposition of 4PADCB induces a blueshift of 0.87 eV relative to bare ITO, indicating electron withdrawal from indium atoms due to SAM adsorption and interfacial dipole formation, originating from either anchoring or hydrogen bonding. In contrast, subsequent washing with 3-FPy produces a modest redshift of 0.12 eV compared to the sample without flush, consistent with partial removal of noncovalently adsorbed species. Meanwhile, 3-MeOPy causes a larger redshift of 0.16 eV, suggesting stronger removal ability.

The UPS data are presented in Figure 4B, and the energy level matching scheme is summarized in Figure 4C. The work function of the control sample (dip-coated only) is measured as 4.47 eV. In comparison, dip-flushed substrates exhibit lower work functions: 4.34 eV for 3-FPy and 4.25 eV for 3-MeOPy. This decrease in work function (i.e., a downward shift of the vacuum level) is attributed to the removal of the dipole layer formed by physisorbed multilayers. Importantly, the ionization energy (IE) of the dip-flushed substrates remains nearly identical to that of the control, indicating that the intrinsic electronic structure of the

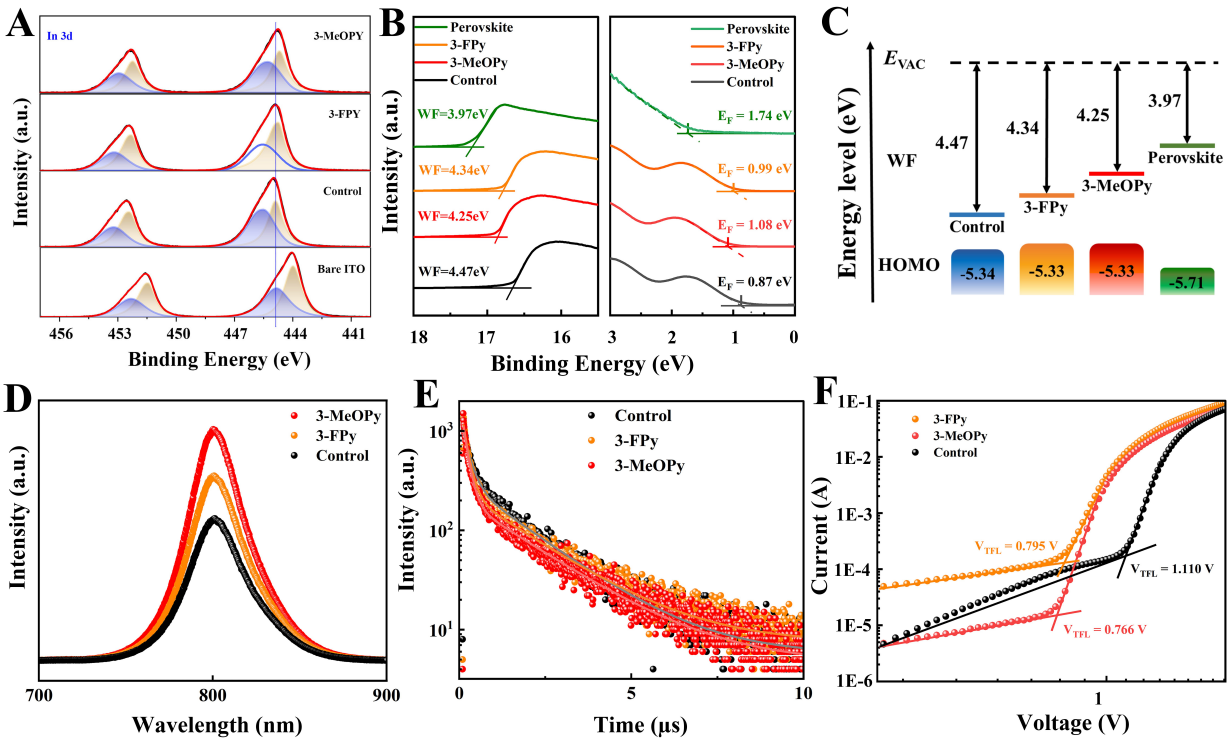


Figure 4. (A) In 3d XPS spectra of SAM-modified ITO substrates. (B) UPS spectra of the SAM substrates and the corresponding perovskite films. (C) Energy level alignment diagram of the SAM/perovskite interface. (D) Steady-state PL spectra of perovskite films deposited on different SAM substrates. (E) TRPL spectra of perovskite films on different SAM substrates. (F) Dark *I-V* characteristics of hole-only devices. 3-FPy: 3-fluoropyridine; 3-MeOPy: 3-methoxypyridine; HOMO: highest occupied molecular orbital; WF: work function; XPS: X-ray photoelectron spectroscopy; SAM: self-assembled monolayer; ITO: indium tin oxide; UPS: ultraviolet photoelectron spectroscopy; PL: photoluminescence; TRPL: time-resolved photoluminescence; *I-V*: current–voltage.

4PADCB molecule is preserved. Consequently, the energy level offset between the dip-flushed SAM and the perovskite is preserved, ensuring that the thermodynamic driving force for hole extraction remains unchanged. Nevertheless, the removal of disordered physisorbed multilayers enhances the morphological quality of the SAM, and this enhancement directly promotes more efficient carrier extraction at the buried interface independently of the energy level alignment.

We employed PL and TRPL measurements on the ITO/SAM/perovskite architecture [Figure 4D and E] to further examine charge extraction and recombination processes. Under top-side excitation, the dip-flushed films show a PL emission that is markedly stronger than that of the control, which directly reflects the enhanced crystallinity achieved with the dip-flush SAM treatment. Turning to bottom-side excitation in TRPL mode, the decay transients were fitted with a biexponential function, where the fast component (τ_1) reflects the interplay of charge extraction recombination, and the slow component (τ_2) is governed by trap-assisted recombination in the bulk and at interfaces, the fitted parameters are summarized in Supplementary Table 1[38-40]. Remarkably, τ_1 progressively shortens from 203.26 ns (control) to 163.15 ns (3-FPy) and further to 153.27 ns (3-MeOPy). This accelerated decay directly evidences enhanced hole extraction at the ITO/SAM/perovskite buried interface, enabled by the removal of physisorbed multilayers. Concomitantly, τ_2 exhibits a marked prolongation: from 1,690.97 ns in the control to 1,855.28 ns (3-FPy) and 1,887.81 ns (3-MeOPy). Such an extended slow lifetime indicates effective suppression of nonradiative recombination, which we attribute to two synergistic effects - the superior crystallinity of the perovskite (as already reflected by the steady-state PL) and, more critically, the elimination of under-protonated P-OH residues that would otherwise serve as defect nucleation sites at the buried interface[2,25]. Collectively, these results underscore that a clean, well-ordered SAM not only boosts interfacial charge extraction but also heals the chemical defect

landscape at the perovskite bottom surface.

To test the impact of the clean SAM on the trap-state density within the perovskite layer, we conducted space-charge limited current (SCLC) measurements on hole-only devices. The current-voltage curves of the hole-only device are illustrated in Figure 4F. The trap-filled limit voltage (V_{TFL}) values extracted from the transition between the Ohmic and trap-filling regions are 1.110 V for the control device, and 0.795 V and 0.766 V for the dip-flushed devices (3-FPy and 3-MeOPy, respectively). Conventionally, the proportionality between the V_{TFL} and trap state density (n_t) is a standard relationship in trap-filled limit analysis, and the lower V_{TFL} in dip-flushed devices therefore confirms a lower trap density, consistent with the removal of under-protonated P-OH groups that otherwise induce defects at the buried perovskite interface[41,42]. These SCLC results align well with the TRPL findings, collectively demonstrating that the dip-flush treatment effectively reduces trap states in the perovskite films.

To evaluate the photovoltaic performance of the dip-flush SAM treatment, we fabricated p-i-n perovskite solar cells with the configuration ITO/SAM/perovskite/PDADI&3MTPAI/C_{60}/BCP/Cu (depicted in Figure 5A). Figure 5B compares the *J-V* characteristics of devices incorporating different substrate modifications. The reference cell, with a dip-coated 4PADCB SAM, delivered a champion reverse-scan efficiency of 25.21%, alongside a short-circuit current (J_{sc}) of 25.65 mA/cm^2, an open-circuit voltage (V_{oc}) of 1.160 V, and a fill factor (FF) of 84.73%. In contrast, the device subjected to 3-MeOPy post-treatment achieved markedly improved metrics: a PCE of 26.49%, V_{oc} = 1.177 V, J_{sc} = 25.81 mA/cm^2, and FF = 87.23%. The hysteresis index (HI) is further calculated to quantitatively assess the *J-V* hysteresis behavior using the commonly adopted equation:

$$\mathrm{HI} = \frac{\mathrm{PCE_{reverse}} - \mathrm{PCE_{forward}}}{\mathrm{PCE_{reverse}}} \times 100\% \quad (3)$$

The HI values of the control and 3-MeOPy-treated devices are 3.57% and 2.00%, respectively, indicating reduced hysteresis after the dip-flush treatment[43,44]. In contrast, devices subjected to IPA and DMSO post-treatment delivered PCEs of 25.80% and 25.59%, respectively, which are considerably lower than those of the 3-MeOPy-treated devices [Supplementary Figure 10], further confirming the specificity of the pyridine-based post-treatment. Steady-state power output (SPO) measurements, shown in Figure 5C, yielded stabilized efficiencies of 26.39% for the dip-flush cell and 25.05% for the control, closely matching their respective *J-V* results. Both cells retained stable performance over 400 s of continuous illumination, indicating good operational robustness. External quantum efficiency (EQE) spectra and their integrated photocurrents are plotted in Figure 5D; the integrated current rose from 25.20 mA/cm^2 (control) to 25.49 mA/cm^2 (dip-flush), in good agreement with the measured J_{sc} values. The statistical distribution of PCEs for the three groups is presented as box plots in Figure 5E (additional parameters are compiled in Supplementary Figure 11). On average, the dip-flush modification raised the PCE to 25.80% for 3-FPy and 26.17% for 3-MeOPy, compared with 24.83% for the untreated control. To test the practical viability of this approach, we fabricated a mini-module with a 12.87 cm^2 aperture area on a 5 cm × 5 cm substrate. As illustrated in Figure 5F, the 3-MeOPy dip-flush module achieved a champion efficiency of 22.56%. The mini-module (active area: 12.205 cm^2; aperture area: 12.87 cm^2) exhibited a geometric fill factor of 94.83%, with only 5.17% area loss from scribing. Collectively, these findings confirm that the dip-flush method is effective not only at the laboratory cell scale but also for larger-area perovskite modules.

To further investigate the non-radiative recombination behavior within the devices, we carried out electrochemical impedance spectroscopy (EIS) and light-intensity-dependent V_{oc} measurements. The EIS results, presented in Figure 5G, reveal that the dip-flush-treated cells exhibit a higher recombination

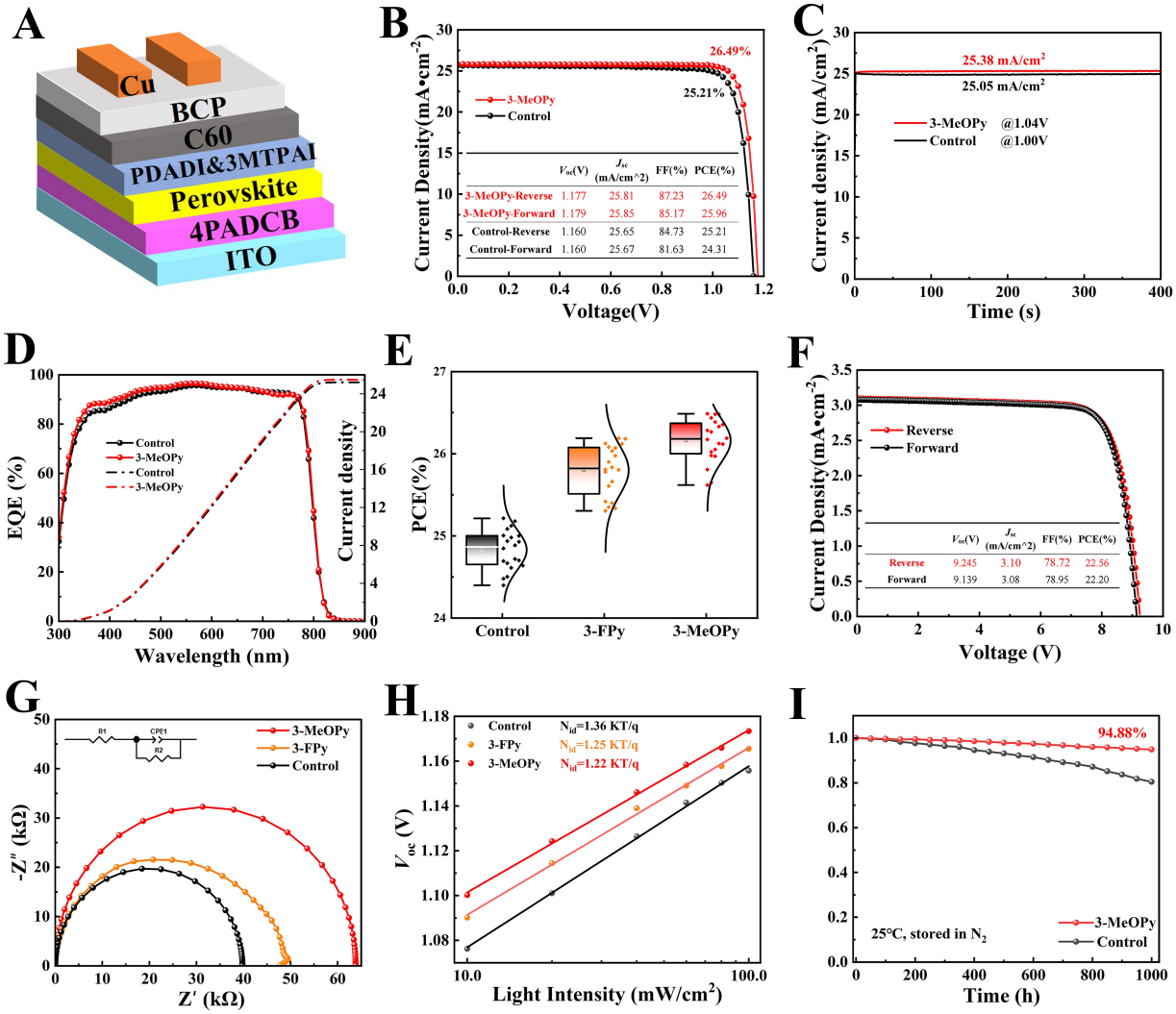


Figure 5. (A) Schematic of the inverted device architecture. (B) *J-V* curves of the champion devices for control and 3-MeOPy-treated SAMs; (C) SPO tracking at the maximum power point for the champion devices over 400 s; (D) EQE spectra and corresponding integrated J_{sc}; (E) Box plots showing the PCE distributions of different conditions based on reverse-scan measurements from 20 independent devices for each condition. The center line, box, and whiskers represent the median, interquartile range (25th-75th percentiles), and data within 1.5× the interquartile range, respectively. (F) *J-V* curve of the champion mini-module with an aperture area of 12.87 cm^2; (G) EIS Nyquist plots, with the equivalent circuit shown in the inset; (H) V_{oc} as a function of light intensity, with the fitted values, $N_{id} = \frac{nKT}{q}$; (I) Stability of unencapsulated devices in the dark under nitrogen atmosphere. BCP: Bathocuproine; PDADI: 1,3-propanediammonium iodide; 3MTPAI: 3-Methylthio-1-propylammonium iodide; ITO: Indium tin oxide; 4PADCB: 4-(7H-dibenzo[c,g]carbazol-7-yl)butyl phosphonic acid; 3-FPy: 3-fluoropyridine; 3-MeOPy: 3-methoxypyridine; EQE: external quantum efficiency; PCE: J_{sc}: short-circuit current; V_{oc}: open-circuit voltage; EIS: electrochemical impedance spectroscopy; SPO: steady-state power output; *J-V*: current density-voltage.

resistance compared with their dip-coating-only counterparts. This observation implies that the dip-flush treatment effectively mitigates non-radiative recombination pathways[45]. Subsequently, we examined the correlation between V_{oc} and illumination intensity, which follows: $V_{oc} = \frac{nKT\ln(L)}{q} + \text{const}$, where n is the ideality factor, K is the Boltzmann constant, T is the temperature, L is the light intensity, and q is the elementary charge[46]. As displayed in Figure 5H, the ideality factor drops from 1.36 (control) to 1.25 for 3-FPy and 1.22 for 3-MeOPy upon dip-flush modification. A reduced ideality factor signifies weakened trap-assisted monomolecular Shockley-Read-Hall (SRH) recombination, confirming that the surface passivation provided by the dip-flush approach is effective in suppressing interfacial SRH losses. Furthermore, the

stability of unencapsulated devices was further evaluated in an N_2 glovebox at 25 °C in Figure 5I. After 1,000 h of aging, roughly 94.88% of the original efficiency was preserved in the 3-MeOPy group, far exceeding the performance of the reference cells. In addition, maximum power point tracking measurements were performed under one-sun white-light light-emitting diode illumination in an N_2 atmosphere at 40 ± 5 °C, as shown in Supplementary Figure 12. After 600 h of continuous operation, the control and optimized devices maintained 41.2% and 83.2% of their initial PCEs, respectively. These results collectively indicate that the flush post-treatment can effectively enhance the device stability.

CONCLUSIONS

In summary, we have developed a dip-flush strategy using pyridine derivatives (3-FPy and 3-MeOPy) to selectively remove physisorbed multilayers from dip-coated 4PADCB SAMs while preserving the chemisorbed monolayer. This post-treatment eliminates under-protonated P-OH residues and yields a clean, well-ordered SAM surface, as confirmed by XPS, AFM, and contact angle measurements. DFT calculations reveal that 3-MeOPy exhibits superior cleaning efficacy due to its stronger hydrogen-bond-accepting ability. The cleaned SAM promotes uniform perovskite crystallization with larger grains and a void-free buried interface, while the unchanged ionization energy maintains the thermodynamic driving force for hole extraction. Consequently, the dip-flush SAM achieves a champion efficiency of 26.49% for small-area devices and 22.56% for a 12.87 cm^2 (aperture area) mini module, demonstrating the applicability of this approach to larger-area device fabrication. This chemically selective strategy provides a scalable route toward high-performance, large-area perovskite photovoltaics.

DECLARATIONS

Authors' contributions

Methodology, formal analysis, and writing of the manuscript: Lei, Y.; Zhong, Q.; Chen, J.
Assisted with experiments and characterization: Li, X.; Yuan, J.; Zhang, J.
Assisted with calculations and theoretical analysis: Hao, L.; Huang, K.; Qian, Y.
Assisted with characterization analysis: Lai, H.; Zhou, X.; Yu, B. B.
Supervision, project administration, and funding acquisition: Chen, J.; Wong, W. Y.; Wang, X.; Liu, C.

Availability of data and materials

The original contributions presented in this study are included in the article/Supplementary Materials. Further inquiries can be directed to the corresponding authors.

AI and AI-assisted tools statement

Not applicable.

Financial support and sponsorship

This work was supported by the National Natural Science Foundation of China (Grant Nos. 62174078 and 62404093), the Natural Science Foundation of Hunan Province (Grant Nos. 2022RC1076, 2023JJ50132, 2024JJ6391, 25RC3191, and 2026JJ20060), the Natural Science Foundation of Guangdong Province, China (No. 2023A1515011637), and the Scientific Research Fund of Hunan Provincial Education Department (Grant Nos. 23A0325 and 25C0244). Wong, W. Y. thanks the financial support from RGC Senior Research Fellowship (SRFS2021-5S01), Research Institute for Smart Energy (CDAQ), and Miss Clarea Au for the Endowed Professorship in Energy (847S).

Conflicts of interest

Chen, J.; Zhou, X. and Liu, C. are affiliated with Hunan Chang-rui New Energy Limited Company, while the other authors have declared that they have no conflicts of interest.

Ethical approval and consent to participate

Not applicable.

Consent for publication

Not applicable.

Copyright

© The Author(s) 2026.

Supplementary Materials

Supplementary Materials

REFERENCES

1. Jiang, W.; Li, F.; Li, M.; Qi, F.; Lin, F. R.; Jen, A. K. π-expanded carbazoles as hole-selective self-assembled monolayers for high-performance perovskite solar cells. *Angew. Chem. Int. Ed. Engl.* **2022**, *61*, e202213560. DOI
2. Li, Z.; Sun, X.; Zheng, X.; et al. Stabilized hole-selective layer for high-performance inverted p-i-n perovskite solar cells. *Science* **2023**, *382*, 284-9. DOI
3. Zhou, H.; Wang, W.; Duan, Y.; et al. Glycol monomethyl ether-substituted carbazolyl hole-transporting material for stable inverted perovskite solar cells with efficiency of 25.52. *Angew. Chem. Int. Ed. Engl.* **2024**, *63*, e202403068. DOI
4. Chen, H.; Liu, C.; Xu, J.; et al. Improved charge extraction in inverted perovskite solar cells with dual-site-binding ligands. *Science* **2024**, *384*, 189-93. DOI
5. Qu, G.; Zhang, L.; Qiao, Y.; et al. Self-assembled materials with an ordered hydrophilic bilayer for high performance inverted perovskite solar cells. *Nat. Commun.* **2025**, *16*, 86. DOI PubMed PMC
6. Qu, G.; Cai, S.; Qiao, Y.; et al. Conjugated linker-boosted self-assembled monolayer molecule for inverted perovskite solar cells. *Joule* **2024**, *8*, 2123-34. DOI
7. Pujari, S. P.; Scheres, L.; Marcelis, A. T.; Zuilhof, H. Covalent surface modification of oxide surfaces. *Angew. Chem. Int. Ed. Engl.* **2014**, *53*, 6322-56. DOI PubMed
8. Li, M.; Liu, M.; Qi, F.; Lin, F. R.; Jen, A. K. Self-assembled monolayers for interfacial engineering in solution-processed thin-film electronic devices: design, fabrication, and applications. *Chem. Rev.* **2024**, *124*, 2138-204. DOI
9. Wang, H.; Wang, J.; He, Q.; et al. Interface dipole management of D-A-type molecules for efficient perovskite solar cells. *Angew. Chem. Int. Ed. Engl.* **2024**, *63*, e202404289. DOI
10. Lenaers, S.; Lammar, S.; Krishna, A.; et al. Pyrene-based self-assembled monolayer with improved surface coverage and energy level alignment for perovskite solar cells. *Adv. Funct. Mater.* **2026**, *36*, 2411922. DOI
11. Liu, T.; Luo, C.; He, R.; et al. Advancing self-assembled molecules toward interface-optimized perovskite solar cells: from one to two. *Adv. Mater.* **2025**, *37*, e2502032. DOI PubMed PMC
12. Yin, R.; Miao, W.; Wang, K.; et al. Coassembled self-assembled monolayers enable efficient and stable inverted perovskite solar cells. *ACS. Nano.* **2025**, *19*, 40345-53. DOI
13. Liu, M.; Bi, L.; Jiang, W.; et al. Compact hole-selective self-assembled monolayers enabled by disassembling micelles in solution for efficient perovskite solar cells. *Adv. Mater.* **2023**, *35*, e2304415. DOI
14. Gao, W.; Dickinson, L.; Grozinger, C.; Morin, F. G.; Reven, L. Self-assembled monolayers of alkylphosphonic acids on metal oxides. *Langmuir* **1996**, *12*, 6429-35. DOI
15. Paramonov, P. B.; Paniagua, S. A.; Hotchkiss, P. J.; et al. Theoretical characterization of the indium tin oxide surface and of its binding sites for adsorption of phosphonic acid monolayers. *Chem. Mater.* **2008**, *20*, 5131-3. DOI
16. Jiang, W.; Qu, G.; Huang, X.; et al. Toughened self-assembled monolayers for durable perovskite solar cells. *Nature* **2025**, *646*, 95-101. DOI
17. Li, G.; Zhang, Z.; Agyei-Tuffour, B.; et al. Stabilizing high-efficiency perovskite solar cells via strategic interfacial contact engineering. *Nat. Photonics.* **2026**, *20*, 55-62. DOI PubMed PMC
18. Lan, Z.; Shao, J.; Zhong, Y. Self-assembled monolayers as hole-transporting materials for inverted perovskite solar cells. *Mol. Syst. Des. Eng.* **2023**, *8*, 1440-55. DOI
19. Yalcin, E.; Can, M.; Rodriguez-Seco, C.; et al. Semiconductor self-assembled monolayers as selective contacts for efficient PiN perovskite solar cells. *Energy. Environ. Sci.* **2019**, *12*, 230-7. DOI
20. Cegiełka, D. M.; Kozieł, K.; Zharnikov, M.; Cyganik, P. Anchoring groups for ordered and highly stable monomolecular films on naturally oxidized aluminum - phosphonate versus carboxylate. *Appl. Surf. Sci.* **2024**, *665*, 160199. DOI
21. Xiang, L.; Yang, X.; Liu, X.; et al. Dip-coating of self-assembled monolayers for perovskite photovoltaic applications. *EcoEnergy* **2025**, *3*, e70007. DOI

22. Mengesha, M.; Alayou, S.; Tizazu, G. Factors influencing surface coverage and structural organization of phosphonic acid self-assembled monolayers on zinc oxide. *Appl. Phys. A.* **2024**, *130*, 8006. DOI
23. Pitaro, M.; Alonso, J. S.; Di, Mario. L.; et al. A carbazole-based self-assembled monolayer as the hole transport layer for efficient and stable $Cs_{0.25}FA_{0.75}Sn_{0.5}Pb_{0.5}I_3$ solar cells. *J. Mater. Chem. A.* **2023**, *11*, 11755-66. DOI
24. Yuan, Z.; Dou, Y.; Liang, J.; et al. Dip-coated SAM/CPA composite hole transport layers for high-efficiency vapor-deposited perovskite solar cells. *Mater. Today. Energy.* **2025**, *50*, 101869. DOI
25. Fei, C.; Zhang, Y.; Wang, M.; et al. Limiting phosphonic acid interlayer-perovskite reactivity to stabilize perovskite solar modules. *Science* **2026**, *391*, eadz7969. DOI
26. Tang, H.; Shen, Z.; Shen, Y.; et al. Reinforcing self-assembly of hole transport molecules for stable inverted perovskite solar cells. *Science* **2024**, *383*, 1236-40. DOI
27. Kresse, G.; Hafner, J. Ab initio molecular dynamics for liquid metals. *Phys. Rev. B. Condens. Matter.* **1993**, *47*, 558-61. DOI PubMed
28. Kresse, G.; Furthmüller, J. Efficiency of *ab-initio* total energy calculations for metals and semiconductors using a plane-wave basis set. *Comput. Mater. Sci.* **1996**, *6*, 15-50. DOI
29. Kresse, G.; Furthmüller, J. Efficient iterative schemes for ab initio total-energy calculations using a plane-wave basis set. *Phys. Rev. B. Condens. Matter.* **1996**, *54*, 11169-86. DOI PubMed
30. Ernzerhof, M.; Scuseria, G. E. Assessment of the Perdew-Burke-Ernzerhof exchange-correlation functional. *J. Chem. Phys.* **1999**, *110*, 5029-36. DOI
31. Grimme, S.; Antony, J.; Ehrlich, S.; Krieg, H. A consistent and accurate *ab initio* parametrization of density functional dispersion correction (DFT-D) for the 94 elements H-Pu. *J. Chem. Phys.* **2010**, *132*, 154104. DOI PubMed
32. Lin, X.; Chen, Z.; Gao, H.; Pan, F.; Wang, X.; Chen, H. the electronic structures and magnetic properties of un-doped In_2O_3: the first-principle calculation. *J. Supercond. Nov. Magn.* **2016**, *29*, 1533-7. DOI
33. Morales, C. A. F.; Pizzo, Z.; Sweeney, D. M.; et al. Multilayer formation, interfacial binding, and stability of self-assembled molecules in perovskite solar cells. *J. Am. Chem. Soc.* **2025**, *147*, 48136-46. DOI
34. Chen, H.; Blatnik, M. A.; Ritterhoff, C. L.; et al. Water structures reveal local hydrophobicity on the In_2O_3(111) surface. *ACS. Nano.* **2022**, *16*, 21163-73. DOI PubMed PMC
35. Kralj, S.; Dally, P.; Bampoulis, P.; Vishal, B.; De, Wolf. S.; Morales-Masis, M. Impact of the TCO microstructure on the electronic properties of carbazole-based self-assembled monolayers. *ACS. Mater. Lett.* **2024**, *6*, 366-74. DOI PubMed PMC
36. Vidyasagar, D.; Yun, Y.; Yu, Cho. J.; et al. Surface-functionalized hole-selective monolayer for high efficiency single-junction wide-bandgap and monolithic tandem perovskite solar cells. *J. Energy. Chem.* **2024**, *88*, 317-26. DOI
37. Luo, C.; Zhou, Q.; Wang, K.; et al. Engineering bonding sites enables uniform and robust self-assembled monolayer for stable perovskite solar cells. *Nat. Mater.* **2025**, *24*, 1265-72. DOI
38. Peng, W.; Mao, K.; Cai, F.; et al. Reducing nonradiative recombination in perovskite solar cells with a porous insulator contact. *Science* **2023**, *379*, 683-90. DOI
39. Li, S.; Jiang, Y.; Xu, J.; et al. High-efficiency and thermally stable $FACsPbI_3$ perovskite photovoltaics. *Nature* **2024**, *635*, 82-8. DOI
40. Zhao, W.; Qu, D.; Zhang, Y.; et al. Photoisomeric molecule-mediated ion anchoring and UV resistance in metal halide perovskites. *Research. (Wash. D. C).* **2026**, *9*, 1196. DOI PubMed PMC
41. Zhang, L.; Fu, M.; Jiang, X.; et al. Benzylphosphonic acid-engineered compact self-assembled monolayers for bifacial buried interface passivation in high-performance inverted perovskite solar cells. *Adv. Sci. (Weinh).* **2025**, *12*, e12117. DOI PubMed PMC
42. Li, C.; Wang, Y.; Gao, W.; et al. Heterointeraction-induced nucleation promoting vertical growth and suppressing phase separation for efficient wide-bandgap perovskite solar cells and tandem devices. *Research. (Wash. D. C).* **2025**, *8*, 0892. DOI PubMed PMC
43. Habisreutinger, S. N.; Noel, N. K.; Snaith, H. J. Hysteresis index: a figure without merit for quantifying hysteresis in perovskite solar cells. *ACS. Energy. Lett.* **2018**, *3*, 2472-6. DOI
44. Rui, Y.; Jin, Z.; Fan, X.; et al. Defect passivation and electrical conductivity enhancement in perovskite solar cells using functionalized graphene quantum dots. *Mater. Futures.* **2022**, *1*, 045101. DOI
45. Yang, L.; Wang, S.; Ma, N.; et al. Modulating binding strength and acidity of benzene-derivative ligands enables efficient and hysteresis-free perovskite/silicon tandem solar cells. *Angew. Chem. Int. Ed. Engl.* **2025**, *64*, e202500350. DOI
46. Cowan, S. R.; Roy, A.; Heeger, A. J. Recombination in polymer-fullerene bulk heterojunction solar cells. *Phys. Rev. B.* **2010**, *82*, 245207. DOI

Disclaimer/Publisher's Note: All statements, opinions, and data contained in this publication are solely those of the individual author(s) and contributor(s) and do not necessarily reflect those of OAE and/or the editor(s). OAE and/or the editor(s) disclaim any responsibility for harm to persons or property resulting from the use of any ideas, methods, instructions, or products mentioned in the content.



© The Author(s) 2026. Open Access This article is licensed under a Creative Commons Attribution 4.0 International License (https://creativecommons.org/licenses/by/4.0/), which permits unrestricted use, sharing, adaptation, distribution and reproduction in any medium or format, for any purpose, even commercially, as long as you give appropriate credit to the original author(s) and the source, provide a link to the Creative Commons license, and indicate if changes were made.